Maxwell-Bloch modeling of x-ray-laser-signal buildup in single- and double-pass configurations

O. Larroche*
CEA DIF, Boîte Postale 12, 91680 Bruyères le Châtel, France

D. Ros, A. Klisnick, A. Sureau, C. Möller, and H. Guennou
LSAI, Université de Paris–Sud, Bâtiment 350, 91405 Orsay Cedex, France

(Received 8 October 1999; revised manuscript received 22 February 2000; published 19 September 2000)

A theoretical model of soft x-ray lasers in hot laser-produced plasmas using a Maxwell-Bloch formalism has been developed and implemented in a numerical code (COLAX). First simulation results in the case of Ne-like Zn from solid targets are presented, including spontaneous emission generation and amplification, refraction, saturation, and coherence properties. A detailed simulation is presented of the effect on amplification and coherence of double-passing the radiation in the amplifying medium by using a half-cavity mirror.

PACS number(s): 42.55.Vc, 42.50.Ar, 52.25.Nr, 42.25.Kb

I. INTRODUCTION: MOTIVATION AND AIM OF THIS STUDY

Several experiments have now demonstrated the potential of using x-ray lasers as a source for exciting solids [1] and for imaging surfaces [2] or dense matter [3–5]. The unique properties of x-ray lasers, as compared with other high brightness x-UV sources, include an exceptionally high number of coherent photons per pulse. In the development of applications where the x-ray laser beam is relayed by one or several optical components (focusing mirror, interferometer, ...) it will be necessary to improve the quality and control of its optical properties, in particular of its coherence. Accounting for the coherence build-up requires detailed modeling, going beyond simple gain estimates relying on Einstein coefficients and radiation transfer arguments, such as those of Ref. [6]. Such refined modeling is expected to reproduce the time-dependent build-up of the x-UV signal including wave coherence properties with an accurate description of refraction and saturation on the inverse-linewidth time scale.

Moreover, in connection with the experiments carried out at LSAI, the model has to include the possibility of using a mirror for double-pass amplification [7,8]. This feature has been shown in experiments to dramatically improve both the output intensity and the coherence properties of x-ray lasers, and this paper presents a detailed simulation of these effects. Optimizing this so-called ''half-cavity'' setup, summarily illustrated in Fig. 1, for the highest coherence, involves simultaneously fine-tuning several geometrical parameters, namely, the radius of curvature of the mirror, its orientation with respect to the plasma axis taking into account the deflection of the x radiation due to refraction inside the plasma, and the position of the mirror with respect to the target. Our code can be of great help in speeding up that optimization process, while reducing the number of trial-and-error cycles in the experimental work, and hence saving laser shots for more productive results.

The active medium of x-ray lasers is a hot plasma with a short life duration, which precludes the large number of cavity round trips typical of visible lasers. X-ray lasers rather work in the so-called ''amplification of spontaneous emission'' (ASE) mode, with possibly a small number of reflections off low-reflectivity x-ray mirrors. Hence the temporal coherence of the x radiation cannot be arbitrarily increased. The spatial coherence, on the other hand, can only be studied through a detailed description of the ASE mechanism and its wave properties.

Previous studies along these lines (see, e.g., Refs. [9–12]) have considered Maxwell-Bloch equations with various limitations. In Ref. [9], paraxial Maxwell equations were numerically solved taking into account a phenomenologically saturated, frequency-independent gain coefficient, thus discarding all time dependencies of atomic quantities on the scale of the inverse linewidth. The more refined model of Ref. [12] actually makes the same assumption. As a consequence, spectral gain narrowing of the line is absent, and the spectral-temporal structure of the signal is not quantitatively accurate. References [10,11] properly take into account all time dependencies (as well as inhomogeneous line broadening in Ref. [11]), but are restricted to the linear small-signal limit where population inversion is unaffected by the x-ray field. An extensive review of theoretical and experimental work on coherent radiation generation in x-ray lasers can be found in Ref. [13].

In this work we improve over Ref. [12] by retaining the complete time dependency of the density matrix for the upper and lower states of the transition in the Bloch equations, and also by using a detailed system of population equations for all levels involved in the pumping mechanism. The rates

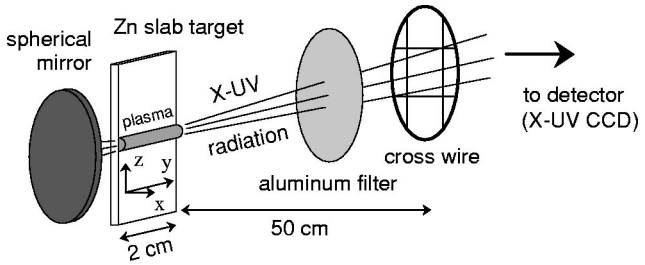

FIG. 1. A schematic of the experimental setup used at LSAI/LULI (see Refs. [7,8] for more detail); also shown is the orientation of the *x*, *y*, and *z* axes of the theoretical and numerical model.

*Electronic address: larroche@bruyeres.cea.fr

required can be obtained from a realistic and quantitative simulation of the atomic physics and hydrodynamics of the system [14]. Our model also takes into account the half-cavity mirror discussed in Ref. [7]. First simulation results are presented in the case of a neonlike Zn laser at 21.2 nm on massive targets.

In this paper we will discuss in detail, in Sec. II, the physical Maxwell-Bloch model used, along with approximations allowed by the orders of magnitude relevant to the x-ray laser case. Some fundamental facts about coherence are gathered in the Appendix. A more detailed account of coherence theory can be found in a basic optics textbook (such as Ref. [15]) or in the review paper of London [16] which also presents a broad overview of existing work in that field. Estimating coherence properties implies a knowledge of the wave electric field, and not only the wave intensity, which makes it necessary to solve Maxwell's equations.

Section III will give a brief account of the numerical methods used in discretizing the physical model, and in Sec. IV simulation results from this code will be presented. This is an ongoing work, for which foreseeable development directions are accounted for in Sec. V.

From the experimental point of view, an x-ray laser coherence measurement has been obtained by Trebes *et al.* [17]. The equivalent source size found was 5 times as large as that calculated with the model of Feit and Fleck [9]. This disagreement might be due to the fact that the measurement was time-integrated while the equivalent source position was changing in the course of time, or to refraction effects not taken into account in the simulation. The complex coherence factor profiles obtained did not depend on plasma length when the latter was increased beyond the saturation threshold.

Another measurement performed at LSAI [18] showed a coherence increase when a mirror was used as indicated in Fig. 1. This work also presented some records of the two-dimensional structure of the x-ray beam in the transverse plane and the dependency of that structure on the mirror settings. These results suggest that a full three-dimensional simulation of the system would be needed for really quantitative predictions, but unfortunately present-day computers only allow us two-dimensional calculations if we want to obtain some useful information in a reasonable amount of computing time.

Reference [19] shows an increase of the transverse coherence length as a function of the radiation amplification distance in a discharge plasma produced inside a capillary. As opposed to Ref. [17], these authors found good agreement of their experimental results with numerical calculations based on the model of Ref. [9].

II. PHYSICAL MODEL

In the case of a localized source, consisting of pointlike elements in vacuum (or in a medium with a constant refraction index), observed from a large distance, elementary considerations about coherence yield an estimation of coherence properties in the radiation utilization region, through the Van Cittert-Zernike theorem (see, e.g., Ref. [15]). In the case of an x-ray laser the situation is more involved since the elementary (spontaneous) radiation is amplified, undergoes refraction, and in addition radiation from different source elements is not independently amplified as soon as the system enters the saturation regime. To estimate the complex coherence factor (defined in the Appendix) in the utilization region, it is thus necessary to calculate the electromagnetic field in a more general way. This implies two types of problems, namely, on one hand, the calculation of the radiation propagation and amplification in an active and inhomogeneous medium, and on the other hand, the description of the initial generation of radiation from elementary sources with correct statistical properties.

A. Evolution of the electromagnetic field

In the limit of a linear polarization along a direction of symmetry z of the problem, the propagation of radiation is governed by the wave equation for the field component E_z deduced from Maxwell's equations, expressed here in cgs units,

$$\frac{-1}{c^2}\frac{\partial^2 E_z}{\partial t^2}+\frac{\partial^2 E_z}{\partial x^2}+\frac{\partial^2 E_z}{\partial y^2}=\frac{4\pi}{c^2}\frac{\partial j_z}{\partial t}+S,$$

where y labels the main propagation direction, x is the transverse direction along which there is an inhomogeneity, and z is the transverse direction of problem symmetry (see Fig. 1). The polarization chosen is the one for which the equations are the simplest to justify rigorously. It will be assumed that the other polarization does not lead to fundamentally different effects, although its governing equations actually display several additional terms with respect to those treated here. The right-hand side has been split into a coherent term involving the current density j_z and a noise source term S.

The current density j_z includes contributions from the motion of free as well as bound electrons (ions are assumed at rest):

$$j_z=j_z^{(f)}+\frac{\partial P_z}{\partial t},$$

where P_z is the dipolar moment density of bound electrons in the direction z. In the linear limit, and if the bulk motion of the plasma can be neglected, the free electron current can be expressed in a simple way as a function of the electric field

$$\frac{4\pi}{c^2}\left(\frac{\partial j_z^{(f)}}{\partial t}+\nu j_z^{(f)}\right)=\frac{\omega_p^2}{c^2}E_z,$$

where ν is an effective collision frequency of free electrons with plasma ions and

$$\omega_p=\left(\frac{4\pi n_e e^2}{m}\right)^{1/2}$$

is the plasma frequency (n_e is the electron density).

B. Evolution of atomic quantities

The quantum states of the system will be split into two sets.

(i) On one hand, a few states whose populations are appreciably affected by population variations on the upper and lower states of the lasing transition considered; the temporal evolution of the populations of these states will be explicitly calculated.

(ii) on the other hand, the set of all other levels, whose populations will be assumed to change little on time scales of the order of the typical radiation evolution time, even when the populations of the upper and lower states of the transition undergo large variations (due, for example, to intensity variations of the corresponding radiation field). The evolution of those levels will thus be satisfactorily described by a standard collisional-radiative model in the frame of the quasistationary approximation.

The evolution of atomic quantities is thus described by equations governing the density matrix elements for the upper and lower states of the transition considered, together with evolution equations for the populations of states which are strongly coupled to those two main states. In the present case, only two states are involved in the stimulated emission process since we consider linearly *z*-polarized radiation on the $J=0-J=1$ line, and a single state of the $J=1$ level is coupled to the $J=0$ state. These equations read

$$\frac{\partial P}{\partial t} = -\gamma P - i\omega D E + \Gamma, \tag{1}$$

$$\frac{\partial \rho_i}{\partial t} = (\delta_{ib} - \delta_{ih}) \frac{1}{2\hbar} \mathrm{Re}(iPE^*) + \gamma_{ij}\rho_j + R_i, \tag{2}$$

where

$$D = \frac{d^2}{\hbar \omega}(\rho_h - \rho_b). \tag{3}$$

In the above equations E and P are the slowly varying complex amplitudes of the electric field and the polarization density, respectively, $E_z = \mathrm{Re}[E(t)e^{-i\omega t}]$ and $P_z = \mathrm{Re}[P(t)e^{-i\omega t}]$, d is the reduced matrix element of the transition dipolar moment, ρ_i is the population of state i in particles per cm^3; summation over index j is implied in the evolution equation for ρ_i. Indices h and b label the upper and lower transition states, respectively, and D is a dimensionless quantity proportional to the population inversion $\rho_h - \rho_b$. ω is the transition frequency and γ is the dephasing rate of the transition atomic dipole (caused by both elastic and inelastic collisions undergone by bound electrons).

In lack of a better description, and according to common practice, the latter quantity will be estimated by the electron-ion Coulomb collision frequency given by

$$\gamma = \nu_{ei} = \frac{4\pi e^4 Z n_e \ln \Lambda_{ei}}{m_e^{1/2}(k_B T_e)^{3/2}} = \nu,$$

where Ze is the ion charge, T_e is the local electron temperature, and $\ln \Lambda_{ei}$ is the Coulomb logarithm defined, e.g., in Ref. [20]. It has been checked in the case of germanium laser-produced plasmas that the Stark broadening due to neighboring ions and electron impact, calculated numerically according to Ref. [21], is negligible for the $3p$-$3s$ transitions in Ne-like Ge^{22+} ions [22]. It is then quite reasonable to assume the same result to apply to Ne-like Zn^{20+} ions. The dephasing rate γ should also take into account the finite lifetime of the states involved, but this contribution was checked to be numerically negligible.

The γ_{ij}'s are the rates (in s^{-1}) of collisional and radiative processes which couple states together, except absorption and stimulated emission processes which are taken into account in a detailed way by the first term of the evolution equation for ρ_i. The R_i (in $\mathrm{cm}^{-3}\,\mathrm{s}^{-1}$) are population fluxes due to collisional and radiative processes involving all other levels of the system. The quantities γ_{ij} and R_i will be provided by the standard collisional-radiative model previously mentioned, since the rates γ_{ij} only depend on intrinsic atomic quantities and slowly varying hydrodynamic quantities (electron density and temperature, etc.), and the fluxes R_i depend on the populations of levels belonging to the set of levels which have been assumed to be slowly varying.

In the above description of the polarization density [Eqs. (1)–(3)], the frequency detuning due to the thermal motion of the ions is not taken into account. As a consequence, only homogeneous line broadening can be treated in this model. Although both homogeneous (namely, lifetime and collisional) broadening and inhomogeneous (thermal) broadening are generally expected to come into play in hot-plasma based x-ray lasers, in the specific case treated in this paper it can be checked from simple order of magnitude estimates that thermal broadening is not expected to be dominant. Measured intrinsic linewidths [23] for these systems lie in the 50 mÅ range, and the expected Doppler width for Zn with an ion temperature around 100 eV (taken from the simulation results [8,24] that we used as described below) is of the order of 15 mÅ. In addition, some experimental results [23] in a very similar case involving neonlike Se ($Z=34$) instead of neonlike Zn ($Z=30$) show that the behavior of the linewidth as radiation is amplified into the saturation regime is actually more faithfully described by a Lorentzian homogeneously broadened line profile, with no rebroadening seen in the strongly saturated regime as should be the case for inhomogeneous broadening. Only part of this discrepancy can be accounted for by a refined, mixed-broadening model such as that presented by Pert [25]. From these facts, it seems reasonable to use a homogeneous broadening formalism as a first step in the description of these systems, with inhomogeneous broadening expected to come into play as a correction only. Taking that correction into account in our code involves a substantial extension of the physical model, and is thus left over for future work, as stated in Sec. V.

The only stimulated transition accounted for in this description is between the chosen states $i=b$ and $i=h$. It is hence assumed that stimulated transitions involving other levels appearing in the above system have negligible rates. This hypothesis is actually not fully valid in the case of the

neonlike ion x-ray laser scheme, in which two transitions, namely, a $J=0-J=1$ line and a $J=2-J=1$ line, sharing the same lower level, are simultaneously amplified with a non-negligible gain. However this situation might still be dealt with through a detailed treatment (by the Maxwell-Bloch system) of one transition while the effect on populations of the other transition would be more summarily described, through a radiation transfer equation. This will be investigated in future work.

The inhomogeneous term involving Γ in the equation for P is a fluctuation term with a very short correlation time, used to model spontaneous emission. Such terms should *a priori* be included in the right-hand side of the equations for the populations ρ_i, but their effect is assumed small with respect to that of the corresponding term in the equation for P. One still has to be aware that *stricto sensu* this might in some cases violate a property of the density matrix which is necessary to ensure population positivity in the numerical code (see Sec. III).

C. Reduced equations

The wave equation for the electric field given in Sec. II A is transformed into paraxial envelope equations by setting

$$E_z(y,x,t)=\mathrm{Re}[E_+(y,x,t)e^{-i\omega t+iky}+E_-(y,x,t)e^{-i\omega t-iky}]$$

where E_+ and E_- are the complex amplitudes of waves propagating in the positive and negative directions respectively along the y axis. E_+ and E_- are slowly varying functions of their three arguments, and k satisfies the dispersion relation of electromagnetic waves in vacuum $\omega=kc$. The polarization density P and noise terms S and Γ are transformed in the same way. We finally obtain

$$\frac{2i\omega}{c}\left(\frac{1}{c}\frac{\partial E_\pm}{\partial t}\pm\frac{\partial E_\pm}{\partial y}\right)+\frac{\partial^2 E_\pm}{\partial x^2}=-\frac{\omega^2}{c^2}(\epsilon_R E_\pm+4\pi P_\pm)+S_\pm, \tag{4}$$

where

$$\epsilon_R=\frac{-\omega_p^2}{\omega(\omega+i\nu)}. \tag{5}$$

ϵ_R is the residual part of the dielectric constant

$$\epsilon=1+\epsilon_R. \tag{6}$$

The first part of the full dielectric constant ϵ has been included in the definition of the envelope approximation. The equations for the polarization density and the atomic populations read

$$\frac{\partial P_\pm}{\partial t}=-\gamma P_\pm-i\omega D E_\pm+\Gamma_\pm \tag{7}$$

$$\frac{\partial \rho_i}{\partial t}=(\delta_{ib}-\delta_{ih})\frac{1}{2\hbar}\mathrm{Re}[i(P_+E_+^*+P_-E_-^*)]+\gamma_{ij}\rho_j+R_i, \tag{8}$$

$$D=\frac{d^2}{\hbar\omega}(\rho_h-\rho_b).$$

The same approximation for neglecting terms involving time derivatives of the slowly varying envelope of the bound electron polarization density has been made as in the case of the free electron current (for a general discussion of this point, see, e.g., Ref. [26]).

When the system evolves slowly with respect to the inverse linewidth, the polarization term in the wave equation can be treated by an adiabatic approximation, which finally yields (see Ref. [27])

$$4\pi P_\pm=\chi E_\pm$$

with

$$\chi=\frac{Q}{\omega-\omega_R+i\gamma},$$

where Q is a real quantity depending on the atomic physics of the problem, and $\hbar\omega_R$ is the energy separation between the upper and lower levels of the transition considered. However, in our case (ASE instead of the evolution of a cavity mode), this is not *a priori* justified and time-dependent equations for matter quantities have to be solved. Using an adiabatic dependency of $P_\pm$ on $E_\pm$ is only valid if the line profile is much narrower than the gain profile or the intrinsic spontaneous emission line profile. Then there must be a way of determining the frequency detuning $\omega-\omega_R$. The arbitrariness in this choice is removed in the usual case of a cavity mode, but in ASE lasers there is no cavity to select a narrow frequency interval, and the model should be able to determine the radiation spectrum from first principles without any arbitrary choice. Actually, the radiation spectrum is expected to spread over a frequency interval of width comparable to that of the gain profile, and taking into account gain-narrowing–rebroadening effects is thus needed to get the correct amplification factor even if one is only interested in the frequency-integrated radiation intensity, as in the case of Ref. [12].

D. Orders of magnitude and dimensionless equations

Equations (4)–(8) will be numerically solved in a rectangular domain modeling the active region of the plasma, with dimensions of the order of a cm in length and a hundred μm in the transverse direction. The x radiation wavelength λ is of the order of ten nm, and the angle α between the propagation direction and the y axis is a few mrad. The field variation scale length in the transverse direction $L_\perp$ is then of the order of

$$L_\perp\approx\frac{\lambda}{\alpha}\approx\text{a few }\mu\text{m}.$$

On the other hand, we know [16] that the longitudinal coherence length is of the order of a hundred μm, which yields the

minimum variation scalelength of the field envelopes E_+ and E_- in that direction, taking into account a minimum growth length of the order of a mm:

$$L_{\parallel} \approx 100 \ \ \mu\text{m}.$$

This implies a numerical grid with at least a few hundred cells in each direction.

If the time step used corresponds to propagation over just one cell in the longitudinal direction, the spontaneous radiation generated at one end of the plasma will then take a few hundred iterations to reach the other end, which will occur in a few tens of ps of time. A few thousand iterations will be needed for a simulation lasting for a typical pump laser pulse duration (a few hundred ps).

In summary, typical maximum values of discretization steps in time and space are of the order of

$$\delta t \approx 100 \ \ \text{fs},$$

$$\delta x \approx 1 \ \ \mu\text{m} \ \ (\text{transverse direction}),$$

$$\delta y \approx 30 \ \ \mu\text{m} \ \ (\text{longitudinal direction}).$$

If we now choose a time unit t_0 of the order of δt and a distance unit $x_0 = c t_0$, Eq. (4) can be rewritten in dimensionless form

$$\frac{\partial E_\pm}{\partial t} \pm \frac{\partial E_\pm}{\partial y} = \frac{i}{2\omega t_0}\frac{\partial^2 E_\pm}{\partial x^2} + \frac{i\omega t_0}{2}(\epsilon_R E_\pm + 4\pi P_\pm) - i\frac{c^2 t_0}{2\omega} S_\pm \tag{9}$$

or, in the adiabatic limit $4\pi P_\pm = \chi E_\pm$,

$$\frac{\partial E_\pm}{\partial t} \pm \frac{\partial E_\pm}{\partial y} = \frac{i}{2\omega t_0}\frac{\partial^2 E_\pm}{\partial x^2} + \frac{i\omega t_0}{2}(\epsilon_R + \chi) E_\pm - i\frac{c^2 t_0}{2\omega} S_\pm . \tag{10}$$

The quantities $E_\pm$ and $P_\pm$ are normalized to a common reference denoted E_0, whose value is not significant up to this point since the equations are linear. In the above equations the first three terms are of order unity in a typical situation. The equations governing matter quantities (which are nonlinear) take on the following dimensionless form

$$\frac{\partial P_\pm}{\partial t} = \omega t_0 \left(-\frac{\gamma}{\omega} P_\pm - i D E_\pm \right) + t_0 \Gamma_\pm , \tag{11}$$

$$\frac{\partial \rho_i}{\partial t} = (\delta_{ib} - \delta_{ih}) \frac{\omega t_0}{2} \left(\frac{dE_0}{\hbar\omega} \right)^2 \text{Re}[i(P_+ E_+^* + P_- E_-^*)] + \gamma_{ij} t_0 \rho_j + \frac{d^2 R_i t_0}{\hbar\omega}, \tag{12}$$

$$D = \rho_h - \rho_b . \tag{13}$$

In Eqs. (12) the populations ρ_i have been adimensionalized by multiplying them by $d^2/\hbar\omega$.

E. Minimal implementation: Quasistationary saturation

A minimal concrete implementation of the code amounts to solving Eqs. (9) and (11) while obtaining the value of the inversion D (along with all atomic and/or hydrodynamic quantities) from code modules which in a first stage will work in the frame of the quasistationary approximation.

In the adiabatic limit, the notion of a linear gain is meaningful; for testing purposes, we will estimate below the population inversion needed to model a given gain value. Inserting the polarization value corresponding to a coherent quasistationary regime for the right-going wave

$$P_+ = -i\frac{\omega}{\gamma} D E_+$$

in Eq. (9), and neglecting diffraction and dispersion effects, we obtain

$$\frac{\partial E_+}{\partial t} + \frac{\partial E_+}{\partial y} = 2\pi\omega t_0 \frac{\omega}{\gamma} D E_+$$

and thus the energy growth rate G (in cm^{-1}) is such that

$$G x_0 = 4\pi\omega t_0 \frac{\omega}{\gamma} D.$$

The dimensionless value of the inversion D leading to a gain value of G cm^{-1} is thus

$$D = \frac{\gamma}{\omega}\frac{G\lambda}{8\pi^2},$$

where λ is the amplified radiation wavelength in cm. Going back to dimensional cgs units, the population inversion needed is

$$\rho_h - \rho_b (\text{cm}^{-3}) = \frac{\hbar}{8\pi^2 d^2}\gamma G \lambda$$

in agreement with Eq. (17) of Ref. [27].

F. Spontaneous-emission modeling

The source terms in the right-hand side of Eqs. (9) and (11) are fluctuation terms responsible for energy injection into the system. According to the literature about the notion of fluctuation-dissipation in atomic systems interacting with radiation (see, e.g., Ref. [28]), the source term in the field equation (9) accounts for the effect of a thermal radiation bath and Bremsstrahlung by plasma particles, and thus is negligible with respect to the effect of the source term in the polarization equation (11). This term will consequently be omitted in the following. In addition, as will be shown further below, only fluctuations on polarization can yield the correct spectral behavior of the field so generated (or in other words, the correct correlation function for the equivalent source term in the field equation), and ultimately the correct intrinsic line profile.

To focus on the effect of fluctuations, we will consider the following simplified system:

$$\frac{dE}{dt} = -\delta E + \alpha P, \tag{14}$$

$$\frac{dP}{dt} = -\beta P + S, \tag{15}$$

where S is a fluctuation term with a very short correlation time with respect to the time scales considered (namely, $1/\beta$ and $1/\delta$ in the above model system); the correlation function of S will thus be assumed in the form

$$\langle S^*(t_1)S(t_2)\rangle = F\,\delta(t_1 - t_2). \tag{16}$$

The damping term $-\delta E$ on the right-hand side of Eq. (14) is intended to model all energy losses, both through electron-ion collisions and through propagation of the field away from the region studied, since spatial dependencies are not explicitly included in this simple model. The correlation function of P can then be calculated from a formal solution of Eq. (15):

$$P(t) = \int_{-\infty}^{t} e^{\beta(t'-t)} S(t')\,dt'$$

$$\Rightarrow \langle P^*(t_1)P(t_2)\rangle = \frac{F}{2\beta} e^{-\beta|t_1 - t_2|}.$$

We thus check that Eq. (14) will be driven by a source term P whose correlation time is the inverse of the intrinsic linewidth.

We can now normalize the P fluctuation term so as to get the right amount of spontaneous emission in E. To this end, we compute the average power injected into the field, from a formal solution of Eq. (14) with no damping term:

$$E(t) = \alpha \int_{-\infty}^{t} P(t')\,dt'$$

$$\Rightarrow \langle |E|^2(t+dt)\rangle - \langle |E|^2(t)\rangle = |\alpha|^2 \frac{F}{\beta^2}\,dt.$$

The spontaneous emission rate is given in cgs units by

$$\frac{d}{d\tau}\frac{\langle \mathcal{E}^2\rangle}{4\pi} = \frac{E_0^2}{8\pi t_0}\frac{d}{dt}\langle |E|^2\rangle = \frac{N\gamma_a \hbar\omega\Omega}{8\pi},$$

where $\mathcal{E}$ and τ are the electric field and time in cgs units, E is the dimensionless complex amplitude of the field propagating in a definite direction ($+$ or $-$), N is the population of the transition upper state in particles per cm^3, γ_a is the global Einstein A coefficient (the inverse of the upper state radiative lifetime) in s^{-1}, $\hbar\omega$ is the energy difference between the upper and lower transition states, Ω is the solid angle into which the modeled radiation propagates and a factor of 2 in the denominator of the latter expression accounts for the fact that E is a single linear polarization component of the field. Comparing the above expressions with one another and inserting the values $|\alpha| = 2\pi\omega t_0$ from Eq. (9) and $\beta = \gamma t_0$ from Eq. (11), we finally obtain the normalization of the fluctuation term to be applied to P [see Eq. (16)]:

$$F = \left(\frac{\gamma}{\omega}\right)^2 \frac{N\gamma_a t_0 \hbar\omega\Omega}{4\pi^2 E_0^2}.$$

This procedure leads to the correct spontaneous emission statistics, assuming the time step to be shorter than the inverse linewidth. In the opposite case (time step longer than the correlation time of the spontaneous emission driving term in E), a fluctuating driving term can be directly applied to E by replacing the correlation function for P derived above with the equivalent delta function. This is consistent with the use of an adiabatic description, if the evolution times found are actually longer than the inverse intrinsic linewidth.

We can now come back to the full Eq. (14) with the damping term included in the right-hand side, and compute the correlation function of the field from the following formal solution:

$$E(t) = \alpha \int_{-\infty}^{t} e^{\delta(t'-t)} P(t')\,dt'.$$

Inserting the formal solution for P obtained above, the field correlation function can be explicitly calculated, with the following result:

$$\langle E^*(t_1)E(t_2)\rangle = \frac{|\alpha|^2 F}{2\beta\delta(\beta^2 - \delta^2)}\left(\beta e^{-\delta|t_1 - t_2|} - \delta e^{-\beta|t_1 - t_2|}\right)$$

and since the damping coefficient δ models the decrease of the field due to propagation, we deduce that it should be of the same order of magnitude as the inverse of the characteristic time scale of the field, or in other words that the equality $\delta = \beta$ should hold. Using this value in the above expression then yields the final result

$$\langle E^*(t_1)E(t_2)\rangle = \frac{|\alpha|^2 F}{4\beta^3} e^{-\beta|t_1 - t_2|}$$

and from the Wiener-Khintchine theorem [15] we are left with the expected Lorentzian line profile with intrinsic width β. In summary, whatever the approximation made, the fluctuating source terms needed always ultimately reduce to random variables with a vanishing correlation time, their correlation function being thus in the form of Eq. (16).

G. Comparison with previous works

In the light of the discussion in preceding sections, we can now come back in more detail to the works cited in Sec. I.

Feit and Fleck [9] solved the paraxial envelope equation (10) with an adiabatic growth rate and a stochastic source term in the right-hand side: this precludes gain narrowing of the laser line since the gain used is frequency independent. Saturation is taken into account in the frame of a quasistationary approximation leading to the classical form

$$G = \frac{G_0}{1 + I/I_{\text{sat}}} \tag{17}$$

where G_0 is the linear, small signal gain and I_{sat} the value of the intensity I for which gain is reduced by a factor of 2 with respect to G_0. This work hence does not describe the polarization density dynamics.

Strauss [10] gave a linear treatment of the Maxwell-Bloch system with a fixed population inversion, including a correct description of temporal dependencies (through an analytical solution of the Laplace-transformed problem). This description applies only as long as the intensity stays away from saturation. This is sufficient for the author's purpose, namely, to show that in a quasi-stationary situation, a correct microscopic description of the linear regime is equivalent on the macroscopic level to a radiation transfer formalism such as that of Ref. [6]. However, the consequence of the quasi-stationary hypothesis with a fixed population inversion is that all effects involving the atomic dipole dynamics are ruled out. This is the adiabatic limit described in Sec. II C.

Working in the same approximation frame, Hazak and Bar-Shalom [11] also obtained an analytical solution of the linear Maxwell-Bloch system (with a fixed population inversion), while in addition taking into account inhomogeneous line broadening. This part of their work will be interesting to us in the envisioned sequels of this work (see Sec. V).

The latter two studies derive analytical results using rather extensive algebra (particularly in Ref. [11] where the problem is expanded into eigenmodes at the cost of lengthy calculations), and their usefulness as a routine experimental optimization tool seems questionable, even though their fundamental physical content and base formalism is relevant.

Garrison *et al.* [12] follow essentially the same lines as Feit and Fleck [9] notwithstanding their preliminary discussion of the Bloch formalism. They actually end using a stationary solution of the equation for the polarization density [Eq. (11) in Sec. II D], which again leads to a frequency-independent gain. As to saturation, the model of Ref. [12] leads to a generalization of Eq. (17) above (which is valid in the stationary limit), including a time dependency of the inversion D which is slow with respect to the field evolution time scale, in the form

$$\tau_0 \frac{\partial D}{\partial t} = D_0 - \left(1 + \frac{I}{I_{sat}}\right) D$$

where D_0 is the weak-signal, unsaturated inversion and τ_0 is the characteristic time for relaxation to a stationary state.

III. DISCRETIZATION

In this section we will briefly summarize the main features of the numerical code which has been developed to implement the theoretical model discussed in Sec. II. A more detailed description of the code will be given elsewhere [29].

All quantities $Q(x,y)$ are discretized on a regular two-dimensional grid (see Fig. 1 for the coordinate axis position):

$$Q_{ji} = Q(x = j\,\delta x,\ \ y = i\,\delta y)$$

for

$$-j_{max} \leqslant j \leqslant j_{max}, \quad 1 \leqslant i \leqslant i_{max}.$$

The numerical solution of Eqs. (9) and (10) uses a time-centered split-step algorithm which separately treats the advection term

$$\frac{\partial E_\pm}{\partial t} \pm \frac{\partial E_\pm}{\partial y} = 0 \tag{18}$$

and the terms accounting for diffraction and matter and radiation coupling

$$\frac{\partial E_\pm}{\partial t} = \frac{i}{2\omega t_0} \frac{\partial^2 E_\pm}{\partial x^2} + \frac{i\omega t_0}{2} (\epsilon_R E_\pm + 4\pi P_\pm + S_\pm), \tag{19}$$

$$\frac{\partial P_\pm}{\partial t} = \omega t_0 \left(-\frac{\gamma}{\omega} P_\pm - iDE_\pm \right) + t_0 \Gamma_\pm . \tag{11'}$$

A scheme which is globally time centered is obtained by successively performing for each time step δt the following operations: (1) solution of the advection equation (18) over a half-time step $\delta t/2$, (2) solution of the diffraction/coupling part (19)/(11′) over a full time step δt; this implies computing D at the intermediate time $t + \delta t/2$, which can only be performed through an iterative solution of Eqs. (12) coupled to (19)/(11′). (3) solution of the advection equation (18) over another half-time step $\delta t/2$.

A stable and sufficiently accurate solution of the advection equation is obtained by a shift and cubic-spline interpolation procedure, with a boundary condition given by the field in the first cell ($i=1$ for E_+, $i=i_{max}$ for E_-). The diffraction and coupling terms are treated by a Crank-Nicholson scheme [30] with a vanishing boundary condition, the reflections off the edges (for $j = \pm j_{max}$) being suppressed by means of a numerical damping term inserted in the right-hand side of Eqs. (9) and (10). The fluctuation source terms are calculated using a random function with a Gaussian law.

The scheme is derived so as to satisfy needed properties of the dissipation-free version of the Maxwell-Bloch system, namely, the energy conservation law, which in dimensionless units reads

$$\frac{\partial}{\partial t} \left(D + \frac{|E|^2}{4\pi} \right) = 0$$

and population positivity ensured by the conservation of the following inequality:

$$|P|^2 \leqslant 4\rho_h \rho_b .$$

Although the scheme is stable regardless of the value of the timestep δt, it is still necessary that δt be smaller than the inverse intrinsic linewidth $1/\gamma$ to avoid an exaggerated gain narrowing, and also, obviously, smaller than the amplification time $2/cG$ (where G is the laser gain); the latter condition is always true in the case of x-ray lasers for the time-step order of magnitude given in Sec. II D.

The mirror used in the half-cavity setup is modeled through a boundary condition on the left edge of the plasma for the right-going field E_+, defined from the retarded outgoing E_- field. The reflection off the mirror *per se* is ana-

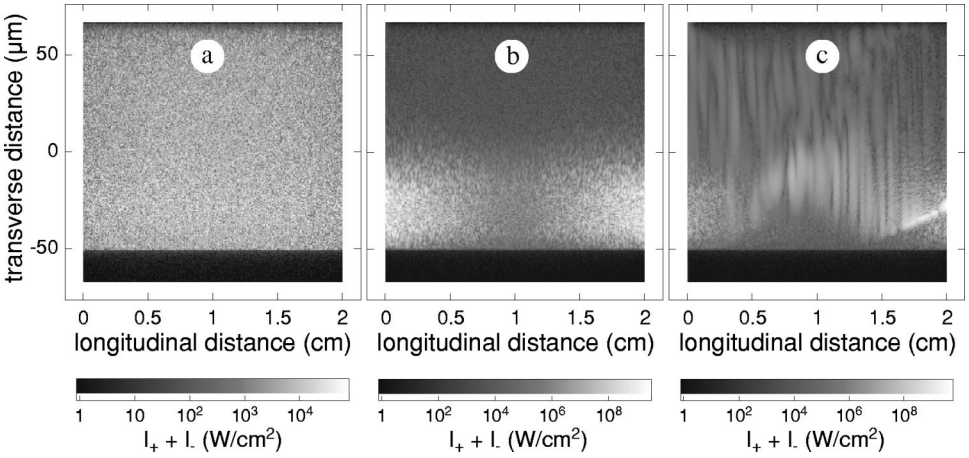

FIG. 2. The total radiation intensity is plotted as a function of distance along (y) and across (x) the plasma at times (a) 50 ps, (b) 200 ps, and (c) 300 ps. The critical density for the 1.06 μm pump laser lies at $x=-50$ μm. The plasma is 2 cm long and a concave mirror faces the left side.

lytically computed from an expansion of the field in vacuum into a superposition of Gaussian beamlets.

IV. SIMULATION PARAMETERS AND RESULTS

Our numerical code COLAX based on the model described above is still under development and the coupling to a hydrocode for a detailed description of the population kinetics is not yet available. Thus as a first validation of our code, we studied the $J=0-1$ transition in neonlike Zn^{20+} using analytical profiles for the hydrodynamic quantities and the inversion density, as deduced from the results of simulations relevant to the experimental conditions [8,24]. We also used a phenomenological saturation intensity as in Refs. [9,12] instead of solving for the full temporal dynamics of the population inversion. With such a simplified model our code is expected to provide more qualitative than accurately quantitative predictions on the field and coherence evolution. The purposes of these first simulations were (i) to study the effect of a half-cavity on the coherence of the double-pass laser beam (see Sec. IV B), (ii) to compare this configuration with a single-pass operation in a plasma twice as long (see Sec. IV C), and (iii) to show how our code can be used to tune the parameters of an experiment for the highest intensity and largest coherence length (see Sec. IV D).

Although the fully developed version of the code could not be tested yet, a benefit of using analytical profiles of the hydrodynamic and atomic parameters is that it allows for a more quantitative validation of the code through a comparison of our results with values which can be estimated by a simple quasi-stationary model using the same analytical parameters.

A. Simulation parameters

The simulation parameters were extracted from the results of Refs. [8,24], which were fitted by temporal and spatial gaussian profiles accounting for the maximum values and widths of the quantities considered. The atomic parameters are as follows (in the reference frame of Fig. 2). The gain profile for the neonlike Zn^{20+} line at $\lambda=21.2$ nm has a 12 cm^{-1} maximum value at $t=200$ ps and $x=-30$ μm, 200 ps FWHM duration and 32 μm FWHM transverse width. The unsaturated upper state population density is $\rho_h=5\times10^{16}$ cm^{-3}. The global Einstein A coefficient is $A=8.7\times10^9$ s^{-1}. The saturation intensity is 9.8×10^9 W/cm^2.

The geometry of the simulated system is as follows: The plasma length is 2 cm. The 30% reflectivity multilayer mirror has a 130 mm curvature radius and its center lies at $x=-920$ μm, $y=+121$ mm. Thus the distance between the plasma end facing the mirror and the mirror surface is 9 mm, which corresponds to a round-trip transit time of 54 ps.

The hydrodynamic parameters are as follows: The electron and ion temperatures used were, respectively, $T_e=300$ eV and $T_i=100$ eV. The electron density profile was modeled by the following expression:

$$n_e(x)=n_{\max}\left\{1-\exp\left[\min\left(0,\frac{x-x_c}{L_s}\right)\right]\right\}+n_c\exp\left(\frac{-(x-x_c)}{L_c}\right),$$

where $n_{\max}=10^{23}$ cm^{-3} is the solid electron density, $n_c=10^{21}$ cm^{-3} is the critical density for the pump laser, $x_c=-50$ μm is the transverse position of the critical surface, $L_s=8$ μm and $L_c=50$ μm are the density gradient scalelengths in the overdense and underdense regions respectively. This expression accounts for both the quasiexponential expansion corona, and a steepening part in denser regions of the plasma beyond critical density.

All simulations were run for 400 ps, which is long enough for radiation to perform a complete round trip in the system including propagation to/from and reflection off the mirror positioned 9 mm to the left of the plasma.

B. Single- and double-pass operation in a 2 cm plasma

Figure 2 displays a map of the total x-ray laser intensity for waves propagating in both directions (i.e., $|E_+|^2+|E_-|^2$, expressed in W/cm^2), in the plasma [i.e., in the (x,y) simulation space], at three different times. At earlier times [$t=50$ ps, Fig. 2(a)] the intensity is dominated by spontaneous emission. Temporal microstructures are seen in the intensity with typical time scales of a few times the inverse-linewidth, as expected. At $t=200$ ps [Fig. 2(b)] amplification of spontaneous emission then leads to an enhance-

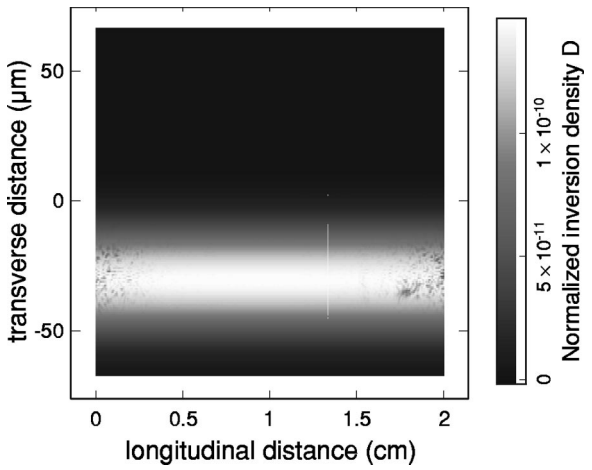

FIG. 3. The normalized inversion density D is plotted as a function of distance along (y) and across (x) the plasma at 250 ps. In addition to the smooth maximum of the modeled small-signal inversion, localized depleted regions due to the effect of stimulated emission appear toward the left and right ends of the plasma.

ment of the intensity at the ends of the plasma. At $t=300$ ps [Fig. 2(c)] the intensity is dominated by radiation reflected by the mirror, leading to smoother ''plane-wave-like'' structures. These structures get amplified and strongly refracted in high-density regions, pointing to the need for an optimization of mirror parameters (radius and center position) in experiments. Intensities of the order of the saturation intensity are reached on the edges of the plasma, in agreement with experimental results as well as simple estimates [8] based on a radiation transfer formalism, thus validating our modeling of spontaneous emission. The onset of saturation shows up as localized regions of depleted inversion in the (x,y) map of the normalized inversion density D in Fig. 3.

Figure 4 shows the mutual intensity $J_{12}(x_1,x_2)=|\langle E_+(x_1,t)E_+^*(x_2,t)\rangle|$ (see the Appendix) of out-going waves at a distance of 50 cm from the right end of the plasma (i.e., $y=52$ cm), for the same times as in Fig. 2. The quantity $J_{12}(x_1,x_2)$ quantifies the correlation of the field for two transverse positions x_1 and x_2 at $y=52$ cm. The angular brackets stand for time integration (over 25 ps in this case). The figures are symmetrical with respect to the diagonal ($x_1=x_2$) line, which displays the variation of the intensity along the transverse direction x. The spatial coherence length $\delta x_{\rm coh}$ can be measured as the distance $|x_1-x_2|$ over which the mutual intensity is decreased by a given factor (2 for example) from its value at a given position x:

$$J\left(x+\frac{\delta x_{\rm coh}}{2},x-\frac{\delta x_{\rm coh}}{2},t\right)=\frac{1}{2}J(x,x,t).$$

At $t=50$ ps [Fig. 4(a)] the coherence length is very small, in relation with the weak amplification exhibited in Fig. 2(a). Later at $t=200$ ps the coherence length becomes appreciable, although still small (of the order of 700 μm). Finally the effect of the mirror is a dramatic coherence increase at $t=300$ ps [$\delta x_{\rm coh}\approx 3.6$ mm, see Fig. 4(c)]. However at that time the x-ray intensity on the recording plane ($y=52$ cm) has decreased with respect to the absolute maximum value recorded at $t=275$ ps. The fact that spatial coherence is largest after the peak of the x-ray laser emission was also experimentally observed in germanium [31].

It should be pointed out that the large coherence increase induced by the half-cavity mirror which is predicted by the code cannot be fully accounted for through geometrical considerations where the equivalent source is in the image plane of the mirror. This increase of the spatial coherence was already observed in our experiments with the double-pass 21.2 nm zinc laser [32]. Diffraction fringes produced by an alignment wire could be recorded only when the half-cavity mirror was used.

C. Single-pass operation in a 4 cm plasma

The coherence increase exhibited in Fig. 4(c) is not simply a consequence of doubling the amplification length by injecting the single-pass radiation back into the plasma. To investigate this point, we performed a simulation using the same parameters as above, except that the plasma length was 4 cm and no mirror was included. Figure 5 displays the intensity map at the time of maximum ($t=300$ ps). As compared to the half-cavity case, the intensity reached at the ends of the plasma in this case is about 10 times as high as the absolute maximum reached at 275 ps, and about 100 times as high as the intensity at 300 ps (see Fig. 2). However, as seen

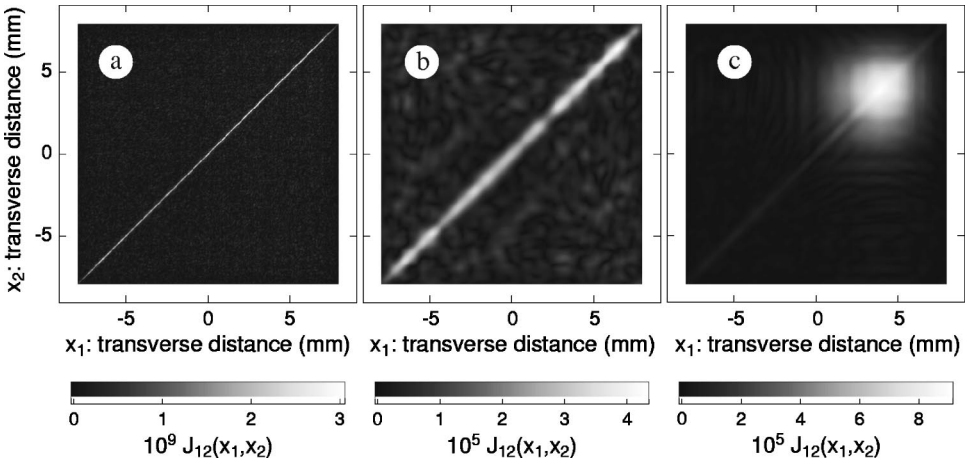

FIG. 4. The mutual intensity $J_{12}(x_1,x_2)$ (in arbitrary units) for a 25 ps integration time on a plane 50 cm away from the right end of the plasma is plotted as a function of x_1 and x_2 at times (a) 50 ps, (b) 200 ps, and (c) 300 ps. The plasma is 2 cm long and a concave mirror faces the left side. The x-scale origin is the same as in Fig. 2.

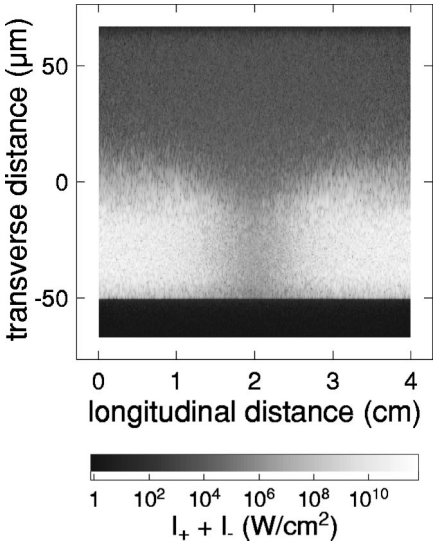

FIG. 5. The total radiation intensity is plotted as a function of distance along (y) and across (x) the plasma at time 300 ps. The plasma length is 4 cm and no mirror is included.

in Figs. 6(a) and 6(b), the coherence length remains significantly shorter, even at later times when the intensity has decreased.

D. Optimization of mirror parameters

The simulation tool described in this paper provides us a means of fine-tuning the parameters of an experiment, particularly the setup of the half-cavity mirror. In experiments performed so far, a concave mirror with parameters as defined in Sec. IV B has been used. We investigated numerically two types of variation of those parameters, namely, a variation of the transverse (x) position of the mirror, other parameters remaining equal to the values given above, and a variation of the focal length of the mirror. These simulations are illustrated in Fig. 7 and Figs. 8,9, respectively.

The variation of the transverse position of the mirror (x_M) yielded a (rather broad) optimum of the x-ray intensity for

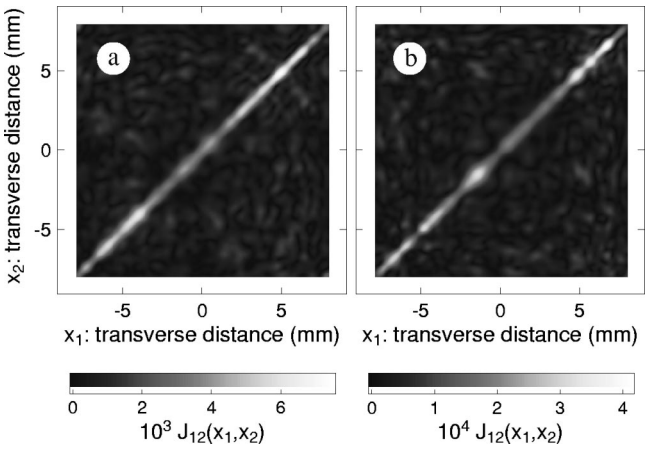

FIG. 6. The mutual intensity $J_{12}(x_1,x_2)$ (in arb. units) for a 25 ps integration time at a plane 50 cm away from the right end of the plasma is plotted as a function of x_1 and x_2 at times (a) 300 ps, (b) 350 ps. The plasma length is 4 cm and no mirror is included.

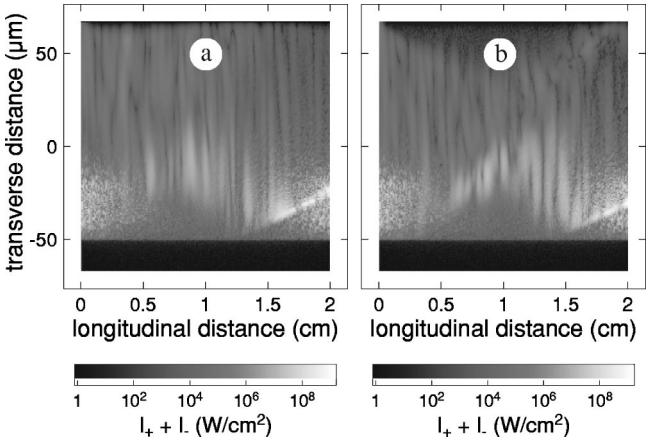

FIG. 7. The total radiation intensity is plotted as a function of distance along (y) and across (x) the plasma at time 300 ps, for cases where the mirror was displaced in the transverse direction with respect to that displayed in Fig. 2(c); here the mirror position was (a) -600 μm and (b) -1100 μm.

the above-defined value ($x_M=-920$ μm). In Fig. 7, intensity maps at 300 ps for $x_M=-600$ μm and $x_M=-1100$ μm are displayed, to be compared with Fig. 2(c). The transverse coherence length at 300 ps, 50 cm away from the plasma was very close ($\approx$3.6 mm FWHM at the position of maximum intensity) for all three cases, and is not shown here.

Various values of the focal length of the mirror were tried, keeping the auto-collimation angle fixed. In Fig. 8 is displayed the case of a concave mirror with a shorter curvature radius (23 mm) than above, with its center of curvature lying in the region where the main part of the x-ray beam gets refracted off the higher-density part of the plasma. Although in this case a larger fraction of the radiation is reflected back into the amplifying region, the maximum intensity inside the plasma and the transverse coherence length at 50 cm to the right are lower than in the case of a plane (or quasiplane) mirror [compare with Figs. 2(c) and 4(c), respectively]. In Fig. 9 are shown the results for a convex mirror with an 18 mm curvature radius, exhibiting an increase of the maximum intensity inside the plasma as well as a larger transverse coherence length [$\approx$5.8 mm FWHM at the position of maximum intensity instead of $\approx$3.6 mm in Fig. 4(c)] with respect to the case illustrated in Figs. 2 and 4.

Further optimization of the experimental setup will be performed using our code, particularly taking into account actual values of mirror parameters and more realistic density profiles for a better simulation of refraction in higher-density regions.

V. SUMMARY AND PROSPECTS

Our Maxwell-Bloch code COLAX describing x-ray laser signal build-up, saturation and coherence using a half-cavity mirror has been successfully tested, and reproduces qualitatively well the coherence increase experimentally observed in double-pass operation. A more detailed version of the code including coupling to simulations of plasma hydrodynamics and population kinetics will be available soon.

The fully time-dependent description of the polarization

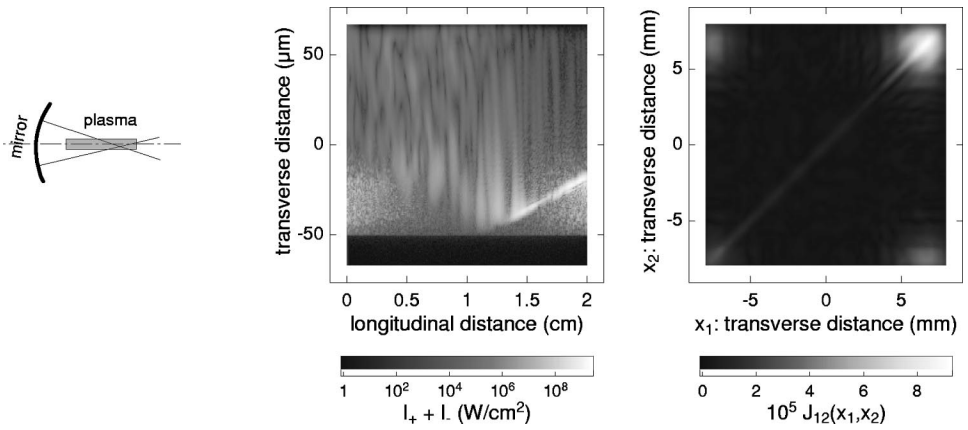

FIG. 8. Simulation results are shown at 300 ps for the case of a concave mirror with the following parameters (see diagram at left): mirror position: -9 mm; position of the curvature center: $x=-42$ μm, $y=14$ mm. On the left is plotted the total radiation intensity as a function of distance along (y) and across (x) the plasma, to be compared with Fig. 2(c); on the right is displayed the mutual intensity for a 25 ps integration time at a plane 50 cm away from the right end of the plasma, to be compared with Fig. 4(c).

density which can be used in the code [Eq. (7)] leads to local x-ray intensities which vary by at most a factor of 2 from their value in the frame of the commonly assumed adiabatic hypothesis, where the instantaneous values of P and the field E are directly proportional. The expected effect of that modeling feature on spectral properties of the laser output (particularly gain narrowing) will be studied in the near future. More dramatic effects might arise when the amplification is larger, and thus the inversion density more strongly saturated than in the cases investigated so far.

Future improvements of the code will include taking into account the $J=2-J=1$ line which is also amplified in the Ne-like scheme, including inhomogeneous broadening and ion diffusion, improving the description of dipole dephasing through a more satisfactory treatment of elastic collisions, extension to the Ni-like scheme, and some approximate modeling of the second transverse (z) direction.

ACKNOWLEDGMENT

We acknowledge support from IDRIS (Institut du Développement et des Ressources en Informatique Scientifique) under Project No. 991043.

APPENDIX: BASIC NOTIONS ABOUT COHERENCE USED IN THIS PAPER

We will give here a very brief account of a few points of coherence theory needed to introduce the quantities used in the main part of this paper. More detailed informations can be found in Ref. [15].

The degree of coherence of a source can be defined as its ability to produce interference fringes in an experiment where it generates two secondary pointlike sources (for example, through diffraction onto the holes in Young's double-hole experiment), whose radiation is superimposed onto a

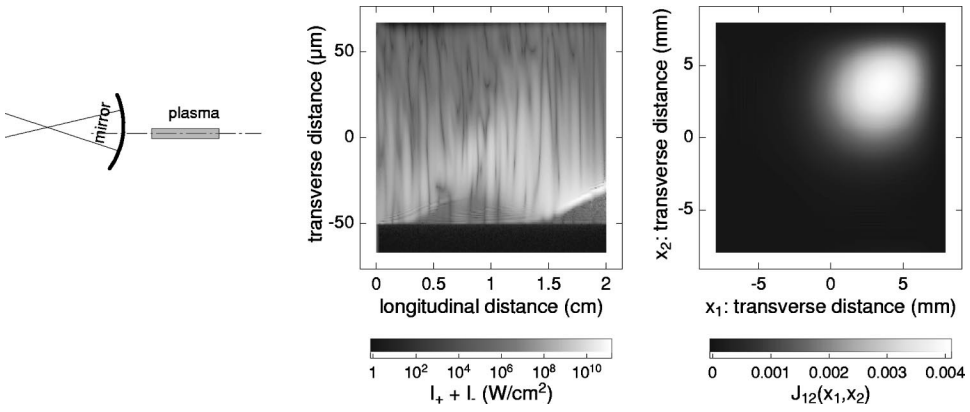

FIG. 9. Simulation results are shown at 300 ps for the case of a convex mirror with the following parameters (see diagram at left): mirror position: -9 mm; position of the curvature center: $x=159$ μm, $y=-27$ mm. On the left is plotted the total radiation intensity as a function of distance along (y) and across (x) the plasma, to be compared with Fig. 2(c); on the right is displayed the mutual intensity for a 25 ps integration time at a plane 50 cm away from the right end of the plasma, to be compared with Fig. 4(c).

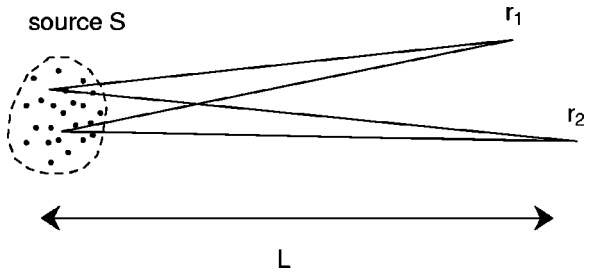

FIG. 10. Coherence is a property of radiation emitted by the source S and recorded in the vicinity of points $\vec{r}_1$ and $\vec{r}_2$.

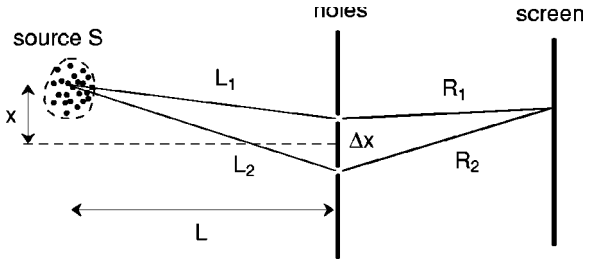

FIG. 11. A schematic Young's holes experiment used to define transverse coherence.

recording device. This notion pertains to the properties of radiation recorded some distance (denoted by L in Fig. 10) away from the source. The primary source is itself considered as a set of pointlike monochromatic source elements, with possibly different frequencies, and well-defined reference phases. The more or less incoherent character of such a source arises from the fact that the mutual phase differences between the source elements of which it is composed are random.

1. Temporal or spatial coherence

Let us denote the positions of the secondary sources by $\vec{r}_1$ and $\vec{r}_2$ (see Fig. 10). Depending on the orientation of the vector $\vec{r}_2-\vec{r}_1$ with respect to the source direction $\vec{S}r$ [where $\vec{r}=(\vec{r}_2+\vec{r}_1)/2$], coherence will be qualified as ''longitudinal'' $[\vec{S}r\|(\vec{r}_2-\vec{r}_1)]$ or ''transverse'' $[\vec{S}r\perp(\vec{r}_2-\vec{r}_1)]$. From the point of view of a single pointlike source element, this means that the phase difference between the waves received at points $\vec{r}_1$ and $\vec{r}_2$ is due to different arrival times or to different propagation directions respectively; coherence can thus also be qualified as, respectively, ''temporal'' or ''spatial.'' In the case of a real extended source, this distinction is less sharp, but still significant as long as the distance L between the source and the recording region remains large with respect to the source dimensions and the recording point separation $|\vec{r}_2-\vec{r}_1|$.

Temporal (or longitudinal) coherence is measured by the distance over which waves emitted by two source elements will get out of phase as a result of their frequency difference. The order of magnitude of this distance is $\lambda^2/\Delta\lambda$ where λ is the center source frequency and $\Delta\lambda$ its spectral width. In practice for the case of x-ray lasers, this distance can be as large as several hundred μm [16]; hence it will be assumed that full temporal coherence is reached is these systems, or in other words that these sources can be considered monochromatic for our purposes.

Spatial (or transverse) coherence is defined as the ability of a source to produce interference fringes in an experiment where it generates two secondary sources lying in a transverse plane, as in Fig. 11. The fringe visibility is proportional to the modulus of the so-called ''complex coherence factor''

$$\mu=\frac{\Gamma_{12}(0)}{[\Gamma_{11}(0)\Gamma_{22}(0)]^{1/2}},$$

where $\Gamma_{12}(\tau)=\langle E(r_1,t)E^*(r_2,t+\tau)\rangle$ is the two-point correlation function of the (linearly polarized) electric field recorded at the location of the holes. In the latter expression, the angular brackets stand for an average over a macroscopic time scale (in practice, the detector integration time). The field $E(r,t)$ is itself the sum of contributions from all source elements. In the above formula, the value $\tau=0$ is used since source monochromaticity (or full temporal coherence) is assumed, as previously explained; in the opposite case a nonvanishing value of τ would account for the different propagation times for waves going through holes 1 or 2.

2. Useful quantities related to transverse coherence

The information conveyed by the complex coherence factor μ just defined can be cast into various forms according to how it is to be used. The simplest of these is the ''mutual intensity'' defined as

$$J_{12}(t)=J(x_1,z_1,x_2,z_2,t)=\langle E(x_1,z_1,t)E^*(x_2,z_2,t)\rangle,$$

where x and z are the transverse coordinates defined in Fig. 1; this is just another notation for the spatial correlation function of the field $\Gamma_{12}(0)$ defined in the previous section.

The most relevant quantity in the case of an experiment producing interference fringes is the fringe visibility, proportional to the difference between the intensity of bright fringes ($I_{\max}$) and that of dark fringes ($I_{\min}$), defined as

$$\begin{aligned}V(x_1,z_1,x_2,z_2,t)&=\frac{I_{\max}-I_{\min}}{I_{\max}+I_{\min}}\\&=\frac{2|\langle E(x_1,z_1,t)E^*(x_2,z_2,t)\rangle|}{\langle|E(x_1,z_1,t)|^2\rangle+\langle|E(x_2,z_2,t)|^2\rangle}\\&=\frac{2J_{12}(t)}{J_{11}(t)+J_{22}(t)}.\end{aligned}$$

Let us recall that in the above expressions, the indices 1 and 2 refer to the locations of the holes in Fig. 11, whereas I_{max} and I_{min} are intensities recorded on the screen lying to the right of the hole plane. Geometrical factors accounting for intensity variations with respect to the direction of propagation from the hole plane to the screen in the diffraction process have been omitted; as a result, the simple expressions given above are strictly valid for small propagation angles only.

[1] P. Jaeglé *et al.*, J. Appl. Phys. **81**, 2406 (1997).
[2] F. Albert *et al.*, Opt. Commun. **142**, 184 (1997); P. Zeitoun *et al.*, Nucl. Instrum. Methods Phys. Res. A **416**, 189 (1998).
[3] E. Wolfrum *et al.*, *X-Ray Lasers 1998*, IOP Conference Series No. 159 (IOP, Bristol, 1999), p. 657.
[4] L. B. Da Silva *et al.*, Phys. Rev. Lett. **74**, 3991 (1995).
[5] A. Klisnick *et al.*, Proc. SPIE **3776**, 282 (1999).
[6] R. A. London, Phys. Fluids **31**, 184 (1988).
[7] B. Rus *et al.*, Phys. Rev. A **55**, 3858 (1997).
[8] B. Rus, Ph.D. thesis, Université de Paris–Sud, Orsay, France, 1995 (unpublished).
[9] M. D. Feit and J. A. Fleck,Jr., J. Opt. Soc. Am. B **7**, 2048 (1990).
[10] M. Strauss, Phys. Fluids B **1**, 907 (1989).
[11] G. Hazak and A. Bar-Shalom, Phys. Rev. A **40**, 7055 (1989).
[12] J. C. Garrison *et al.*, Phys. Rev. A **43**, 4941 (1991).
[13] P. D. Gasparyan, F. A. Starikov, and A. N. Starostin, Phys. Usp. **41**, 761 (1998).
[14] P. B. Holden *et al.*, J. Phys. B **27**, 341 (1994).
[15] M. Born and E. Wolf, *Principles of Optics* (Pergamon Press, London, 1964).
[16] R. A. London, Phys. Fluids B **5**, 2707 (1993).
[17] J. E. Trebes *et al.*, Phys. Rev. Lett. **68**, 588 (1992).
[18] F. Albert, Ph.D. thesis, Université de Paris–Sud, Orsay, France, 1998 (unpublished).
[19] M. C. Marconi *et al.*, Phys. Rev. Lett. **79**, 2799 (1997).
[20] D. V. Sivukhin, *Coulomb Collisions in A Fully Ionized Plasma*, Vol. 4 of *Reviews of Plasma Physics*, edited by M. A. Leontovich (Consultants Bureau, New York, 1966), p. 93.
[21] B. Talin *et al.*, Phys. Rev. A **51**, 1918 (1995).
[22] D. Benredjem *et al.*, Phys. Rev. A **56**, 5152 (1997).
[23] J. A. Koch *et al.*, Phys. Rev. A **50**, 1877 (1994).
[24] S. Jacquemot, in *X-Ray Lasers 1994*, edited by David C. Eder and Dennis L. Matthews, AIP Conf. Proc. No. 382 (AIP, Woodbury, NY, 1994), p. 279.
[25] G. J. Pert, J. Opt. Soc. Am. B **11**, 1425 (1994).
[26] A. Yariv, *Quantum Electronics* (Wiley, New York, 1987).
[27] A. Sureau and P. B. Holden, Phys. Rev. A **52**, 3110 (1995).
[28] See, e.g., H. Haken, *Laser Light Dynamics*, Vol. 2 of *Light* (North Holland, Amsterdam, 1985).
[29] O. Larroche (unpublished).
[30] J. Crank and P. Nicholson, Proc. Cambridge Philos. Soc. **43**, 50 (1998).
[31] R. R. Burge *et al.*, J. Opt. Soc. Am. B **15**, 1620 (1998).
[32] A. Klisnick *et al.*, in *Lasers '94*, edited by V. J. Corcoran and T. A. Goldman (STS Press, McLean, VA, 1995), p. 69; see also Ref. [7].